ADVANCED FUNCTIONAL MATERIALS
www.afm-journal.de

Water Confinement in Nitrogen-Rich Nanoporous Carbon Materials Revealed by In Situ Scanning Transmission X-Ray Microscopy

*Bin Wu, Faidra Amargianou, Jan-David Förster, Christopher Pöhlker, Thomas Guy Rauch, Deniz Wong, Christian Schulz, Robert Seidel, Markus Weigand, Martin Oschatz, and Tristan Petit**

The interaction between water molecules and surfaces in porous carbon-based materials plays a significant role in various fields including but not limited to catalysis, gas sorption, or electrochemical energy storage and conversion. The incorporation of nitrogen enhances the hydrophilicity of typically rather nonpolar carbon-based materials but the molecular understanding of water chemical configuration in such porous materials remains incomplete. Water adsorption on nitrogen-containing nanoporous carbon surfaces is governed by a subtle balance between water–water and water–surface hydrogen bonding interactions, which together determine the water structures formed and their stability. In this work, in situ Scanning Transmission X-ray microscopy performed on individual nanoporous carbon particles under a humid atmosphere is used to elucidate the interactions between nitrogen-containing carbon surfaces and water molecules. The hydrogen bonding of water is found to be nonuniform within the particles and to depend on the nanopore size and the chemical bonding of nitrogen atoms. The nature of the nitrogen sites interacting with water is further characterized by resonance inelastic X-ray Scattering and near ambient pressure X-ray Photoelectron Spectroscopy. This study provides new perspectives on water interaction when confined in nanoporous nitrogen-rich carbons.

1. Introduction

Interactions between water molecules and surfaces are among the fundamental phenomena in electrochemical energy devices.[1,2] Interfacial water found at electrode–electrolyte interfaces has a crucial influence on the performance of energy storage devices such as aqueous electric double-layer capacitors for electrochemical energy storage[3,4] or electrocatalysts for energy conversion.[5,6] In the context of nanoporous materials, confinement in the pores may change the local ordering or density of the confined water molecules.[7] This, in turn, may bring new opportunities for chemical nanoreactors.[8]

Nanoporous carbon materials provide high surface area, electrical conductivity, and high thermal/chemical stability. This makes them promising, amongst others, for applications in catalysis, atmospheric water capture, and energy storage.[9–11]

B. Wu, F. Amargianou, T. G. Rauch, D. Wong, C. Schulz, R. Seidel, M. Weigand, T. Petit
Helmholtz-Zentrum Berlin für Materialien und Energie GmbH
Albert-Einstein-Straße 15, 12489 Berlin, Germany
E-mail: tristan.petit@helmholtz-berlin.de

B. Wu
Institute of Physics
Humboldt University Berlin
Newton-Straße 15, 12489 Berlin, Germany

The ORCID identification number(s) for the author(s) of this article can be found under https://doi.org/10.1002/adfm.202406528

[+]Present address: Atmospheric Microphysics Department, Leibniz Institute for Tropospheric Research, Permoserstraße 15, 04318 Leipzig, Germany

DOI: 10.1002/adfm.202406528

F. Amargianou
Faculty of Mathematics and Natural Sciences
TU-Berlin, Hardenbergstr. 36, 10623 Berlin, Germany

J.-D. Förster[+], C. Pöhlker
Multiphase Chemistry Department
Max Planck Institute for Chemistry
Hahn-Meitner-Weg 1, 55128 Mainz, Germany

M. Oschatz
Institute for Technical Chemistry and Environmental Chemistry
Friedrich-Schiller-University Jena
Philosophenweg 7a, 07743 Jena, Germany

M. Oschatz
Center for Energy and Environmental Chemistry Jena (CEEC Jena)
Philosophenweg 7a, 07743 Jena, Germany

M. Oschatz
Helmholtz Institute for Polymers in Energy Applications Jena (HIPOLE Jena)
Lessingstraße 12–14, 07743 Jena, Germany

Their huge specific surface area as well as tunable pore size distribution ensure excellent electrochemical activity in aqueous systems and their electrical conductivity allows for a limited ohmic drop during electrochemical polarization. This qualifies carbons, amongst other high-current applications, as an electrode of choice in electrochemical double-layer capacitors.[12,13] For applications in heterogeneous electrocatalysis such as electrochemical oxygen reduction and evolution, a large electrochemically active surface area is highly desired. Furthermore, the hydrophilicity and electroconductivity of carbon materials can be tuned through doping with other elements such as nitrogen into the carbon framework, or by modification of their surface chemistry with specific functional groups.[14,15] To control the chemical constructions of carbon materials as precisely as possible, thermal condensation of precursor substances toward "molecular carbon materials" is one suitable approach.[16] For instance, a template-free synthesis of nanoporous carbon materials with high and controllable nitrogen content by direct condensation of the hexaazatriphenylene (HAT-CN) precursor (C-HAT-CN) was recently reported.[17] C-HAT-CN materials belong to the family of C_2N-type compounds and have demonstrated extremely high hydrophilicity with favorable adsorption profile of water and several gases as well as attractive electrocatalytic properties.[18–20] Especially, the water adsorption properties of these C-HAT-CN materials are remarkable with heats of adsorption significantly above the evaporation enthalpy of bulk water over a very broad range of uptakes and appear to be more typical for zeolite materials rather than for classical porous carbons.[17,21,22] Theoretical calculations also indicated high adsorption affinity of the C-HAT-CN materials toward H_2O and underlined the importance of the interplay between basic pyrazinic nitrogen atoms and nearby positively polarized carbon atoms as surface active sites for water adsorption.[23] Nevertheless, a molecular understanding of the water structure and the nature of its chemical bonding with nitrogen sites remains elusive.

Several analytical methods have been applied to elucidate the water hydrogen bonding (H-bonding) in porous and carbon-based materials. For instance, Nuclear Magnetic Resonance (NMR) spectroscopy allows a precise identification of water H-bonding because the chemical resonances are sensitive to the change of electron density and chemical environments of the investigated nuclei.[24] In addition, Fourier Transform Infrared Spectroscopy and Raman spectroscopy are highly sensitive to the water H-bonding networks,[25–27] but it remains difficult to apply them on strongly absorbing porous carbon particles. Furthermore, intense research with contradicting findings has been carried out recently to study the structure and orientation of water molecules on carbon surfaces based on vibrational sum-frequency-generation spectroscopy, however also limited to flat carbon surfaces (graphene).[28–30]

Core-level soft X-ray spectroscopies are element-specific techniques that allow to probing separately the carbon, nitrogen, and oxygen electronic states. Near Ambient Pressure X-ray Photoelectron Spectroscopy (NAP-XPS) has been used to study the water interaction with diamond[31] and carbon nitride surfaces,[32] but cannot access the inner nanopores due to its short probing depth. X-ray Absorption Spectroscopy (XAS), on the other hand, also offers high sensitivity to the local chemical environment but with bulk sensitivity when transmission detection is used.[26] XAS at the oxygen K-edge was found to be highly sensitive to the H-bonding of interfacial water on colloidal carbon nanomaterials.[33,34]

In this work, we provide a molecular understanding of water adsorption in porous nitrogen-rich carbon particles using in situ Scanning Transmission X-ray Microscopy (STXM). STXM allows the monitoring of water H-bonding in individual C-HAT-CN particles by acquiring XAS with sub-50 nm spatial resolution. The carbon, nitrogen, and oxygen bonding environments in C-HAT-CN prepared at different condensation temperatures exposed to helium with relative humidity (RH) up to 80% at room temperature were characterized by in situ STXM. Clear inhomogeneities of the H-bonding for water confined close to the surface and in the core of individual C-HAT-CN particles were observed. Moreover, the nature of the nitrogen sites interacting with water molecules was further characterized by NAP-XPS and Resonant Inelastic X-ray Scattering (RIXS), identifying the critical role of pyridinic nitrogen in the water adsorption process. This work provides new chemical insights into the role of nanoconfinement and nitrogen on the zeolite-like water adsorption properties of nanoporous nitrogen-rich carbon materials.

2. Results and Discussion

2.1. Carbon and Nitrogen Bonding in C-HAT-CN Materials

The series of model C-HAT-CN materials described in the following has been prepared by thermal condensation of HAT-CN at 550, 700, and 1000 °C, and the resulting porous nitrogen-carbon materials are denoted as C-HAT-CN-550, C-HAT-CN-700 and C-HAT-CN-1000, respectively. Our earlier studies[17,21] have shown that a temperature of 550 °C is needed to induce condensation of HAT-CN to a microporous framework at reasonable rates and that the ideal condensation degree and a stoichiometry of nearly perfect C_2N is reached at 700 °C. For comparison with another microporous carbon material with significantly lower nitrogen content, we have also introduced C-HAT-CN-1000 as a reference sample in the present study. Specifically, in this series of samples, it has been found that the specific surface areas slightly increase from 627 to 785 m^2 g^{-1} and 801 m^2 g^{-1} for C-HAT-CN-550, C-HAT-CN-700, and C-HAT-CN-1000, respectively. At the same time, micropore volumes also slightly increase from 0.24 cm^3 g^{-1} (C-HAT-CN-550) to 0.30 cm^3 g^{-1} (C-HAT-CN-700) and 0.31 cm^3 g^{-1} (C-HAT-CN-1000) due to a slight enlargement of the micropore size. Arther pronounced differences are found in the atomic C/N ratios in the materials determined from combustion elemental analysis which are 1.64, 1,96, and 13.83 for C-HAT-CN-550, C-HAT-CN-700, and C-HAT-CN-1000, respectively.

For the present study, the chemical composition of the C-HAT-CN particles was first explored by STXM at C and N K-edges. **Figure 1a** displays the STXM images at the C K-edge of individual C-HAT-CN-700 particles. The core and surface regions (Figure 1b) are isolated based on their chemical bonding using a clustering analysis (see Supporting Information for details). STXM images at the C K-edge for C-HAT-CN-550 and C-HAT-CN-1000 particles are shown in Figure S2 (Supporting Information).

The XAS at the C K-edge of the three C-HAT-CN samples obtained by averaging the transmitted X-rays in the surface and core

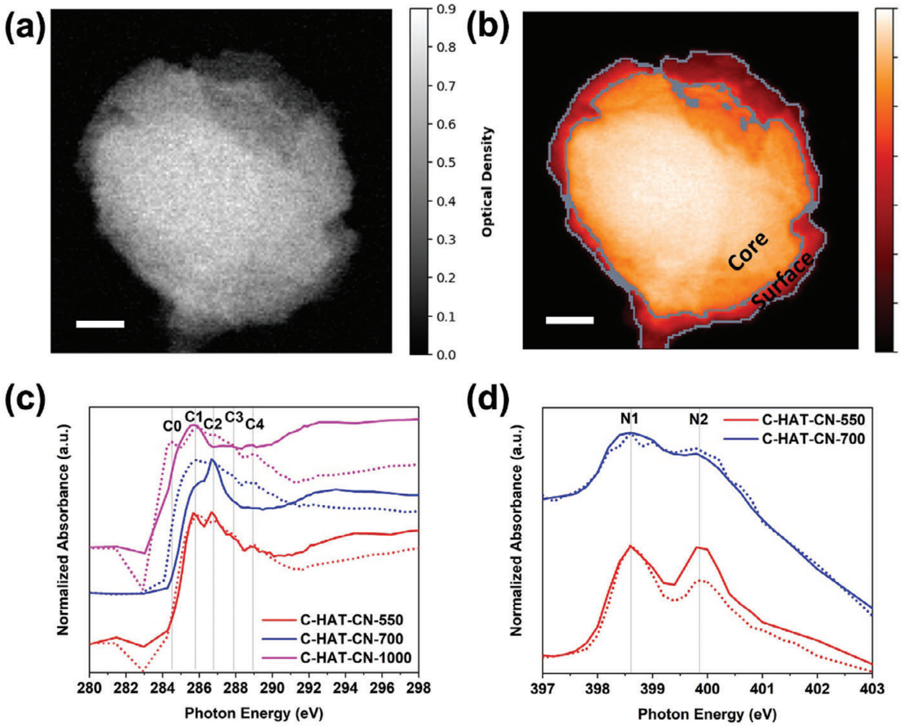

Figure 1. Carbon and nitrogen bonding in individual C-HAT-CN-700 particles. a,b) STXM images under dry conditions as well as core and surface regions of the clusters at 285 eV (C K-edge) of the C-HAT-CN-700 sample. The scale bars are 2 µm. XAS at C K-edge c) and N K-edge d) of C-HAT-CN-550, C-HAT-CN-700, and C-HAT-CN-1000 for the core (dotted line) and surface area (solid line). All spectra were normalized to the XAS pre-edge and shifted for clarity.

regions exhibit two main features in the pre-edge at ≈285.8 eV (C1) and ≈286.8 eV (C2), for C-HAT-CN-550 and C-HAT-CN-700 (Figure 1c). The feature C1 is related to transitions from C 1s to $\pi^*_{C=C}$ orbitals, mostly coming from graphitic carbon while C2 is assigned to transitions from C 1s to the $\pi^*_{C\equiv N}$ orbital in the terminal cyano group.[35] The C2 feature is not observed on C-HAT-CN-1000 which is completely condensed. Smaller contributions at ≈287.9 eV (C3) and ≈ 289 eV (C4) are also visible. C3 is attributed to the transition to π^*_{C-N-C} in the pyridine-like ring of a matrix, which also appears in the C_3N_4 system.[36,37] In addition, C4 can be assigned to transitions from C 1s *to* $\pi^*_{C=O}$, suggesting the presence of O-containing functional groups and defects,[37] as confirmed by the XAS O K-edge discussed later. For C-HAT-CN-1000, an additional peak C0 located at 284.7 eV is detected. It is associated with transitions to π^*(aromatic carbon),[38] suggesting the presence of highly graphitized carbon in C-HAT-CN-1000 compared to the particles obtained by condensation at lower temperatures, which is in line with the characterization from previous studies.[17,21] The core region appears more graphitized than the surface of the particle. Note that a saturation of the carbon signal is observed for the core region due to the large thickness of the particle and the relative intensity of the peaks cannot be reliably compared.

The XAS at the N K-edge of the different C-HAT-CN samples extracted from the STXM images (Figure S3, Supporting Information) are shown in Figure 1d. Note that no nitrogen was detected on C-HAT-CN-1000, which is in line with the absence of C—N bonding (C2) in C K-edge XA spectra, and low nitrogen content detected by XPS (<8 at.%) and elemental analysis (<5 at.%) in similarly prepared material reported in previous work.[17] Two main features are detected at ≈398.6 eV (N1) and ≈399.8 eV (N2) on C-HAT-CN-550 and C-HAT-CN-700. The feature N1 is related to π^* transition of pyridinic N and N2 is associated with the excitation from N 1s to $\pi^*_{C\equiv N}$ orbital in the cyano group.[35,39,40] The assignment to the cyano group was further confirmed using RIXS at the N K-edge (Figure S4, Supporting Information) as discussed in the Supporting Information. The nitrogen bonding appears quite homogeneous across the particles and the slight peak intensity changes may be related to a thickness-induced saturation of the X-ray absorbance.

2.2. Nitrogen–Water Interaction at Near Ambient Pressure of Water

The chemical change of the nitrogen sites upon exposure to water was first probed by NAP-XPS. The N 1s spectra of the C-HAT-CN-700 in vacuum show two main components, which are attributed to pyridinic N at 399.25 eV and cyanic N at 401.40 eV binding energy, respectively (**Figure 2**).[41] Another weaker component at 403.56 eV can be attributed to oxidized pyridinic N. When exposing the sample to 1–3 mbar of water under near ambient pressure (NAP) conditions, both components shift by 0.6 eV (pyridinic N) and 0.2 eV (cyanic N) toward lower binding energies. The larger shift for the pyridinic N peak suggests a chemical interaction with water, possibly through electron delocalization between the

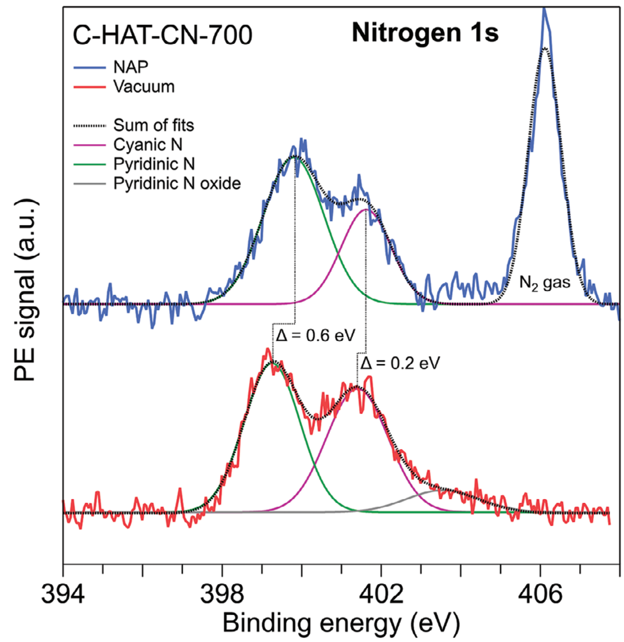

Figure 2. N 1s XP spectra of C-HAT-CN-700 at vacuum and NAP conditions (≈1 mbar water vapor) at an excitation photon energy of 700 eV. Spectra have been background-subtracted and energy-calibrated against Fermi (Figure S5, Supporting Information). Peaks have been fitted by Gaussians representing the cyanic N, pyridinic N, and pyridinic N oxide as well as nitrogen gas. After applying NAP conditions, the main peaks are shifted toward lower binding energies.

pyridinic nitrogen and condensed water molecules. The pyridinic N oxide peak is not detected under NAP conditions. The water condensation on the surface of C-HAT-CN-700 is further confirmed by recording the partial electron yield X-ray absorption (PEY-XA) spectra at the oxygen K-edge (Figure S6, Supporting Information).

The photoemission spectra (PES) obtained for resonant excitation of the different nitrogen states identified with XAS at the N K edge provide further insights into the chemical interaction between nitrogen atoms and water molecules. **Figure** 3a,b show 2D maps corresponding to the valence band spectra recorded as a function of the excitation photon energy for C-HAT-CN-700 under vacuum and NAP conditions. At first glance, both contour plot representations look quite similar except in the region highlighted in the dashed white ellipses corresponding to N1s2p2p resonant Auger electron decay channel (Figure 3a,b). The decay channel at 399 eV is less intense than the one at 400 eV, especially under NAP. When the maps are integrated along their binding energy axis, PEY-XA spectra are obtained. Two peaks related to the excitation of an N 1s electron to the π^* orbitals of pyridinic N (at 399 eV) or to the cyanic group (at 400 eV) are observed, as for transmission XAS (Figure 1d). However, when normalizing both PEY-XA spectra (Figure 3c,d), the peak at 399 eV appears clearly less intense for NAP compared to vacuum conditions. From a fitting of the XAS, the relative area of the pyridinic compared to the cyanic component decreases of 45% upon interaction with water (Figure S7 and Table S1, Supporting Information). We attribute this decrease to a strong orbital hybridization between the π^* orbitals of pyridinic N and water. Due to the hybridization, the excited electron has a chance to delocalize with the water environment during the few femtosecond N1s core-hole lifetime and is therefore no longer available for a refill of the core-hole with a subsequent resonant Auger electron decay. In contrast, the intensity of the cyanic N absorption peak is hardly affected, because there is no spatial overlap between the cyano groups and water, and therefore no hybridization could occur. This interpretation is also supported by resonant valence band photoelectron (RPE) spectra at 399 and 400 eV photon energy discussed in the Supporting Information (Figure S8, Supporting Information). These resonant photoemission results therefore demonstrate a strong chemical interaction between water and pyridinic nitrogen upon exposure to water molecules. These interactions go far beyond typical physisorption schemes and are mainly responsible for the high hydrophilicity of these N-rich carbon materials.

2.3. Water Adsorption in Individual C-HAT-CN Particles

The electronic structure of the water condensed inside the pores of the C-HAT-CN particles was then investigated by in situ STXM. Individual C-HAT-CN particles are exposed to helium with up to 80% RH and monitored continuously inside an in situ STXM microreactor.[42] Hyperspectral STXM images at the carbon, nitrogen, and oxygen K-edges were collected at increasing RH for C-HAT-CN-550, C-HAT-CN-700, and C-HAT-CN-1000 samples. No clear changes are observed at the carbon and nitrogen K-edges for low humidity (Figure 1) and high humidity (Figure S1, Supporting Information). Unlike AP-XPS discussed earlier, which is only sensitive to the first few nanometers, all nitrogen atoms are probed in transmission XAS. As such, we can conclude that most of the nitrogen atoms contained in C-HAT-CN are not in contact with the water molecules therefore after averaging over all nitrogen atoms, no change is detected. On the other hand, significant changes are observed at the oxygen K-edge as a result of water adsorption within the particles. The oxygen optical density (OD) extracted from the STXM images at 535 eV excitation energy increases significantly with humidity (**Figure 4**). The water adsorption seems to saturate at ≈60% RH for C-HAT-CN-1000 while the OD continues to increase up to the maximal probed RH for the other samples.

The spatial distribution of adsorbed water within C-HAT-CN-700 at low humidity (RH < 5%) was analyzed in further detail (**Figure 5**). We distinguished surface and core regions using a cluster analysis based on their XA spectra signature (see Figure S4, Supporting Information and details in Supporting Information). Four main components are observed in the XAS at the O K-edge in the surface region for all samples at low RH (**Figure 5**). The details of the fitting parameters are given in Table S2 (Supporting Information). Feature O1 originates from C=O bonding, suggesting the existence of some oxygen-containing functional groups for all samples.[43] The features O2–O4 are related to water molecules with different H-bonding configurations. In general, the XAS of liquid water consists of a pre-edge at 535 eV (O2), a main edge at ≈537 eV (O3), and a post-edge at 540 eV (O4).[44,45] O2 originates from uncoordinated OH groups due to unsaturated or dangling hydrogen bonds on the H-donating site. O3 is also related to the population of molecules with unsaturated H-bonds, while O4 is associated with the fully saturated

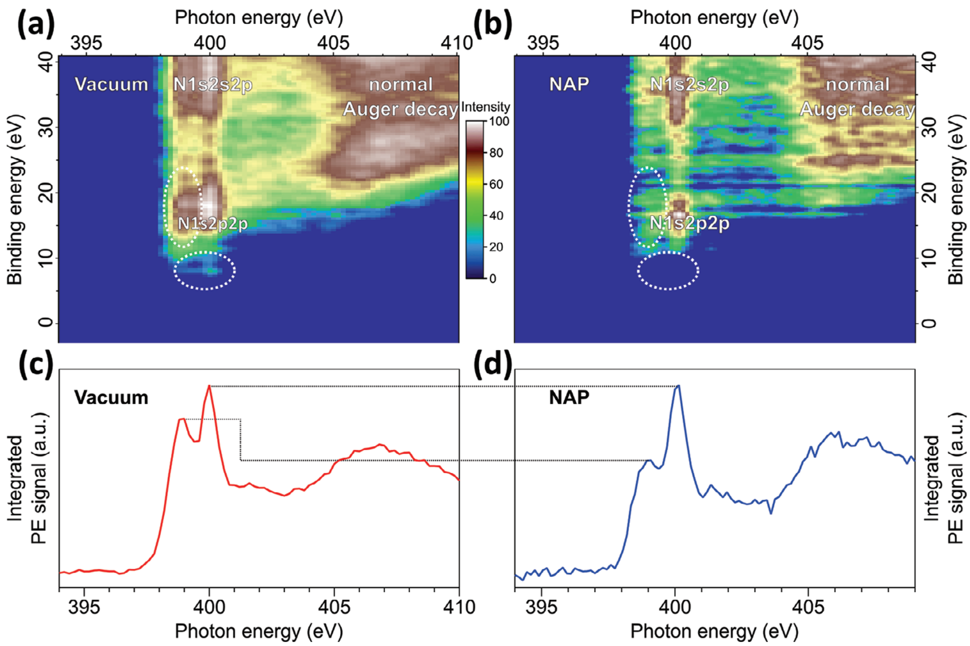

Figure 3. Resonant valence band spectra near the nitrogen K-edge. a) Contour plot from C-HAT-CN-700 at vacuum conditions. b) Contour plot from C-HAT-CN-700 at NAP conditions. The electron signal intensity is expressed by a color code (blue – lowest intensity, white – largest intensity). For both maps, an off-resonant valence PES measured at 395 eV photon energy, slightly below the N 1s resonance, has been subtracted from each individual spectrum. Dashed white ellipses indicate missing intensity in the NAP spectra. c,d) PEY-XA spectra obtained by integration along the binding energy axis of the contour plots in vacuum c) and NAP d).

H-bonding network.[44] An additional O' band seems to be present at 543 eV in the core region of C-HAT-CN-550 and C-HAT-CN-700 (Figure 5d,e). The attribution of this feature may tentatively be attributed to σ^*_{N-O}.[43] It cannot be distinguished in the XAS of C-HAT-CN-1000 because of the presence of overlapping and broader O4 combined with the low nitrogen content.

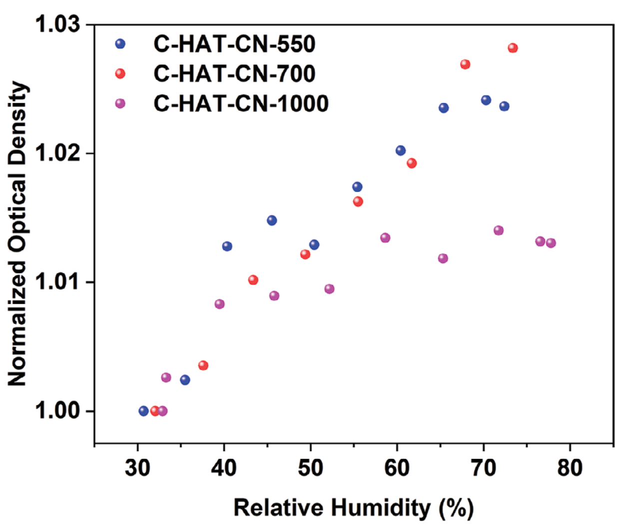

Figure 4. Water adsorption on individual C-HAT-CN particles. The optical density (OD) averaged over the full particle imaged by STXM is monitored at 535 eV as a function of humidity in the in situ STXM microreactor. The OD was normalized to the minimum OD of each sample.

Water molecules are observed in C-HAT-CN even at low RH conditions at room temperature, which is reasonable because of their strong water adsorption capability, which necessitates heating above 200 °C in an inert atmosphere to remove all water molecules.[17] By comparing the spectral shape of the O2–O4 components to previously reported XAS O K-edge of water molecules in another environment, one can estimate the nature of the water H-bonded network in the porous particles. In the core region, the O2 and O3 peaks are predominant, similar to water monomers adsorbed on metal surfaces.[46] The O2 and O3 correspond to the $4a_1$ and $2b_2$ orbitals of water molecules, which are broadened and energy-shifted compared to the gas-phase molecules due to the hybridization with the pyridinic groups of the C-HAT-CN surface. For C-HAT-CN-1000, the appearance of the O4 post edge shows the presence of strongly H-bonded water molecules. Due to the much lower nitrogen content, water molecules are not stabilized by pyridinic groups and may form H-bonds between each other, hence forming small water clusters with dominating water-water interactions, interacting less with the carbon surface. In the surface region, the post edge O4 is dominating for all samples, with an increasing relative area for higher condensation temperature. This is related to strong H-bonding donating interactions by H_2O monomers, forming a more extended H-bonding network but still weaker than in bulk water.[47]

The evolution of water H-bonding with increasing humidity was then monitored by recording the XAS at the O K-edge over the same particles. When the RH increases, the water-related O2–O4 features become more intense (Figure 5g–i). The O1 peak related to C—O bonds on the C-HAT-CN surface does not change and is used as a reference for XAS normalization. Most of the

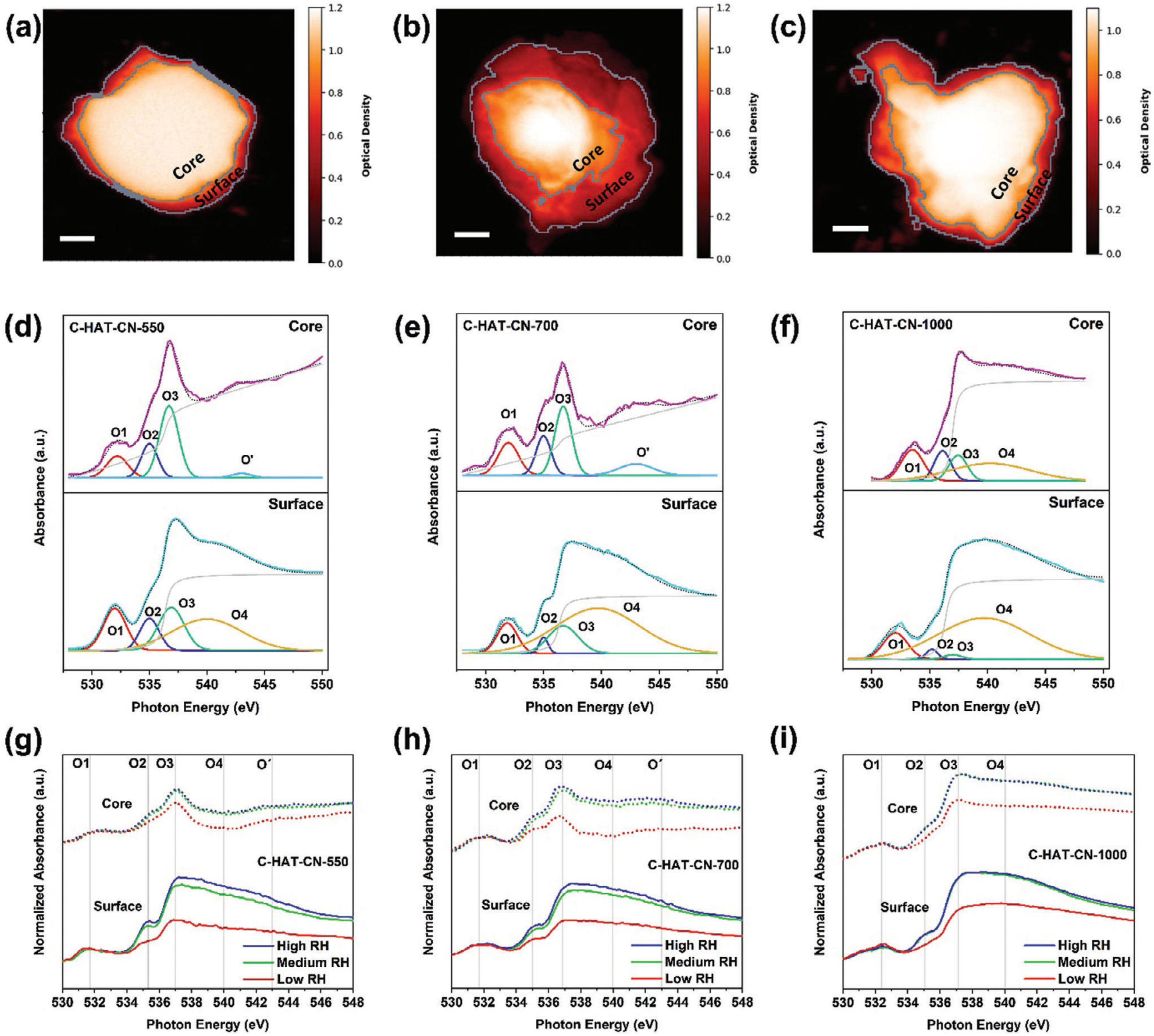

Figure 5. Water adsorption in individual C-HAT-CN particles monitored by in situ STXM. STXM images at O K-edge (at 535 eV) under low RH for C-HAT-CN-550 (RH = 1.9%) a), C-HAT-CN-700 (RH = 4.9%) b) and C-HAT-CN-1000 (RH = 4.5%) c). The scale bars are 2 µm. The peak fitting of XAS at O K-edge for two regions of core and surface area with distinct spectral behavior at low (<5%) RH are shown for d) C-HAT-CN-550 e) C-HAT-CN-700 and f) C-HAT-CN-1000 samples. XAS at O K-edge for two regions of core and surface area with distinct spectral behavior at low (<5%), medium (≈30%), and high (≈75%) RH are compared for g) C-HAT-CN-550 h) C-HAT-CN-700 and i) C-HAT-CN-1000 samples. The dotted lines represent the XA spectra at the core area and solid lines correspond to the XA spectra at the surface region. All the spectra were normalized to the XAS pre-edge and offset for clarity.

X-ray absorption increase occurs below RH 40%, especially for the core regions. The spectral shapes at medium and high humidity are similar and overlap in the case of C-HAT-CN-1000, indicating the saturation of water absorption at relatively low RH, as discussed earlier (Figure 4).

The pre/main-edge ratios of the XAS at the O K-edge were analyzed to qualitatively estimate the evolution of the H-bonding network of water molecules in the C-HAT-CN samples with humidity (**Figure 6**). At low humidity, in the surface (core) region of C-HAT-CN-550, C-HAT-CN-700, and C-HAT-CN-1000, ratios of 0.58 (0.60), 0.46 (0.53) and 0.42 (0.44), respectively, were calculated. The ratios decreased by 14 (9), 9 (6), and 8 (6) % at surface (core) regions, respectively, at high RH compared to those at low RH, suggesting a strengthening of the H-bond network for increasing the number of adsorbed water molecules. Furthermore, under both high and low RH, the pre/main-edge ratio is higher in surface regions compared to core regions for all samples, showing a stronger H-bonding in the core of C-HAT-CN materials. Moreover, with the increase of condensation temperature, the ratio of pre/main edge decreases in both surface and core area

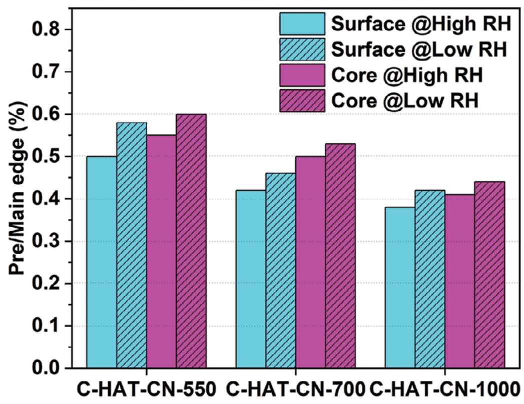

Figure 6. The ratio of the pre/main edge of the XAS at the O K-edge was obtained from in situ STXM recorded on individual C-HAT-CN particles under low and high humidity for core and surface area.

as follows: C-HAT-CN-550 > C-HAT-CN-700 > C-HAT-CN-1000 (Figure 6). Comparing these values to the reported pre/main-edge ratio of 0.38 for liquid water,[48] we can conclude that the H-bonding network in the pore of all C-HAT-CN materials remains generally weaker than bulk liquid water even at high RH. The same H-bonding as liquid water is reached only in the surface region of the C-HAT-CN-1000 sample at high RH.

2.4. Discussion

Based on these spectromicroscopic results, a molecular description of the structure of water adsorbed and confined in the pores of C-HAT-CN mesoporous materials is proposed as summarized in **Figure 7**. The chemical interaction with the pyridinic groups, as well as the pore confinement, are both affecting the water organization in the nanopores. As found by NAP-XPS, a higher nitrogen content leads to a stronger contribution of chemical interactions (i.e., electron transfer and the formation of joint orbitals) between pyridinic groups and water molecules, which does not occur for graphitic carbon. This result agrees with theoretical calculations, suggesting a high adsorption affinity of C-HAT-CN for water molecules due to the activation of the lone pairs of the pyridinic nitrogen atoms.[23] H-bond formation between water and pyridinic groups may lead to the breaking of hydrogen bonds between water molecules in the first adsorption layers.[49] There are thus fewer water molecules in the double H-bond donor configuration, which is confirmed by the absence of the O4 post edge feature in XAS O K-edge obtained at core regions of C-HAT-CN-700 and C-HAT-CN-550.[50] For C-HAT-CN-1000 with lower nitrogen content but still, with a porous structure, the hydration of the pores is more likely to resemble liquid water as observed in carbon nanotubes and other graphitic nanostructures. For example, Molinero et al. investigated water–graphite interaction via molecular simulation[51] and concluded that liquid water at the surface of the graphite interface has similar free energy, entropy, and enthalpy as bulk water. This is highly consistent with our observation on C-HAT-CN-1000 at high humidity.

The averaged pore size of C-HAT-CN-1000, C-HAT-CN-700, and C-HAT-CN-550 was previously determined to be 1.5, 1.1, and 0.8 nm, respectively, by gas physisorption.[17] Considering the diameter of one water monomer which is in the order of 0.3 nm, the slight pore differences between the different samples may accommodate much larger water clusters. The fact that the H-bonding is less distorted for the C-HAT-CN-1000 compared to C-HAT-CN-550 and C-HAT-CN-700 can result from both a lower nitrogen content and from larger pores.

The difference between core and surface regions within one particle may be explained by a slightly different pore structure and lower accessibility of the core regions to the water molecules. In the surface region, a gradual strengthening of the water H-bonding is observed with increasing humidity. The generally stronger water H-bonding in the surface region may suggest that larger pores are formed there, facilitating the formation of more ordered water clusters with localized H-bonds compared to a core region with smaller pores where only water monomers can be adsorbed. Unfortunately, the spatial resolution of STXM is not high enough to visualize the pores and their connectivity within the mesoporous carbon and the gas physisorption only provides an average pore distribution, without information on the pore distribution within individual particles. Another possible interpretation for the different water H-bonding between surface and core regions would be that once the surface pores are fully saturated with water molecules, diffusion of additional water molecules to the core is inhibited. This phenomenon would mean that the water molecules cannot diffuse through the porous channels above a certain RH and only monomers strongly interacting with the C-HAT-CN surface, already present at low RH, are found in the core region. Both size-limited and diffusion-limited H-bonding could explain the weaker H-bonding network in the core region

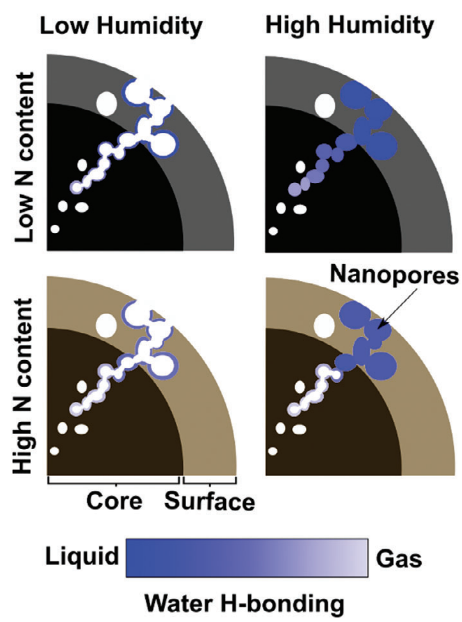

Figure 7. Schematic picture of water adsorption in mesoporous carbon materials. Surface regions are shown with lighter colors. Pores, particles, and water layers are not at scale. For clarity, only one porous channel is drawn. The filling of the pores by water molecules is indicated in blue color while the strength of the water H-bonding between gas-like water monomers and liquid-like condensed water is qualitatively indicated according to the scale bar.

of the C-HAT-CN. The characterization of porous carbons with varying pore size distribution and similar surface chemistry may clarify this latter point in future studies.

3. Conclusion

In this work, we probed the H-bonding of confined water in mesoporous nitrogen-containing materials. To this aim, the electronic structure of confined water was probed by XAS at the oxygen K edge on individual particles for varying humidity using in situ STXM. Different H-bonding between water molecules confined in the surface and core region of the C-HAT-CN materials were observed. The differences in the H-bonding motifs are explained by different pore sizes and nitrogen content which are controlled by the C-HAT-CN synthesis temperatures. In addition, the inhomogeneous chemistry and/or pore size between surface and core regions also affects the water adsorption. Pyridinic nitrogen was found to undergo significant chemical interaction with adsorbed water molecules based on NAP-XPS and XAS. This work highlights that the specific chemical construction of porous carbon-nitrogen compounds can be used to achieve a fine-tuning of the water microenvironment in their pores.

4. Experimental Section

Synthesis of HAT-CN: The synthesis of hexaazatriphenylenehexacarbonitrile (HAT-CN) was carried out according to the procedure stated in the literature.[17] Briefly, Hexaketocyclohexane octahydrate (4 g, 12.6 mmol) and diaminomaleonitrile (10.88 g, 100.8 mmol) were refluxed in AcOH (150 mL) for 2 h. The black suspension was filtered off while hot and washed with hot AcOH (3 × 25 mL) resulting in a black solid. The solid was suspended in 30% HNO_3 (60 mL) and heated at 100 °C for 3 h. The hot dark brown suspension was poured into ice water (200 mL) and cooled overnight. The suspension was filtered and the solid was refluxed in MeCN (400 mL) for 2 h and was filtered. The filtrate was evaporated in vacuo to give an orange solid.

Synthesis of C-HAT-CN-X: In a typical procedure, C-HAT-CN-X was prepared using HAT-CN (500 mg) for condensation in a horizontal tubular furnace at different temperatures for 1 h under N_2 gas flow. The heating ramp was set up to be 2 °C min^{-1} from room temperature to 80 °C, and 4 °C min^{-1} from 80 to 550, 700, or 1000 °C, respectively. The resulting materials described are C-HAT-CN-X, where C stands for condensed and X is the synthesis temperature.

Scanning Transmission X-ray Microscopy: STXM imaging was conducted at the UE46-PGM2 undulator beamline at the BESSY II synchrotron at the "MAXYMUS" endstation with a provided energy range of 130–2000 eV. It provides a resolution of $E/\Delta E \leq 8000$ at C and the measurements were conducted in single-bunch top-up mode.[52] A zone plate was used with a 25-nm outer zone width in whose point focus the sample, mounted on a piezo stage, was scanned by moving it perpendicular to the beam direction, while the order-sorting aperture between the zone plate and sample prevents the sample from being hit from zero-order light. The total transmitted beam was detected with a fast avalanche photodetector, allowing one to extract spatially resolved spectroscopic information with a good signal-to-noise ratio as well as to perform time-resolved microscopy. The STXM-NEXAFS data analysis was conducted using the Multivariate ANalysis Tool for Spectromicroscopy software (MANTiS-3.0.01). This included the extraction of spectra, the map creation, and the cluster analysis (CA). MANTiS-compatible files were compiled from the filtered reconstructions via custom-made scripts, programmed in Python 3.6.5.[53]

Resonant Inelastic X-Ray Scattering: RIXS measurements were performed at the U41-PEAXIS beamline using the endstation PEAXIS of BESSY II.[54] The samples were prepared using the same procedure as for XAS. The RIXS spectra were acquired with an incident angle of 30° from the sample surface and a scattering angle, 2θ, of the detector at 60°. Carbon tape optimized the instrument resolution to 60 meV at the N K-edge.

Near-Ambient Pressure X-ray Photoemission Spectroscopy: NAP-XPS measurements were carried out at the U49/2-PGM-1 beamline at BESSY II using the near-ambient pressure SOL^{3}PES experimental setup, which is equipped with a Scienta Omicron R4000 HIPP-2 hemispherical electron analyzer. There are three differential pumping sections, each consisting of a pinhole and two molecular turbo pumps, to separate the detector unit from the experimental chamber. A similar differential pumping scheme is used to deal with the pressure difference between the experimental chamber and the ultra-high vacuum ($<10^{-9}$ mbar) inside the beamline. During the measurements, the angle between the polarization axis of the incoming soft X-ray and the electron analyzer was 54.7° (magic-angle geometry) to avoid any photoelectron angular distribution effects. PE measurements were performed at high vacuum (between 8×10^{-5} and 6×10^{-6} mbar) and NAP conditions (between 1 and 3 mbar). The distance between the electron analyzer entrance pinhole and the focal point of the soft X-ray beam was shorter than 500 μm, minimizing electron scattering at elevated water vapor pressure in the chamber that causes an attenuated electron signal. To create the water vapor environment, a test tube was connected and filled with ultrapure water (degassed by two freeze-pump-thaw cycles) to the vacuum chamber. A needle valve was used to set the required H_2O gas flow into the chamber. The pumping flow rate is controlled with a motorized gas-regulating valve (Pfeiffer EVR 116), which was managed by a proportional-integral-derivative controller (Pfeiffer RVC300 pressure gauge). Additionally, a temperature-controlled chiller (Julabo F12-ED) actively cooled the sample holder. The U49/2 beamline provides high-brilliant soft X-ray light up to a photon energy of Eph = 1400 eV, enough to core-ionize oxygen and carbon. The energy resolution of the beamline was better than 220 meV at 400 eV photon energy used for the absorption spectra, and better than 500 meV at 700 eV photon energy for the N1s XPS measurements. The energy resolution of the electron analyzer was 250 meV (pass energy of 100 eV). The measured photoelectrons had kinetic energies between 300 and 400 eV, which translates to an electron inelastic mean free path range of ≈3–4 nm.[55] The recorded N1s spectra were energy-calibrated against the Fermi edge and measured separately after each scan (Figure S7, Supporting Information).

Supporting Information

Supporting Information is available from the Wiley Online Library or from the author.

Acknowledgements

This work was supported by the Volkswagen Foundation (Freigeist Fellowship No. 89592) and CSC scholarship (No. 201904910594). The authors thank the Helmholtz-Zentrum Berlin für Materialien und Energie for the allocation of synchrotron radiation beamtime. Dr. Wuyong Zhang and Dr. Mingren Liu (both from FSU Jena) are acknowledged for materials synthesis. R.S. acknowledges funding from the Deutsche Forschungsgemeinschaft (DFG, German Research Foundation) through an Emmy-Noether Grant (SE 2253/3-1). M.O. acknowledges the financial support by the German Federal Ministry of Education and Research (BMBF) in the project "Hydrogen Storage in Nanowater" (03SF0737A "WaNaWa") within the Ideenwettbewerb "Wasserstoffrepublik Deutschland."

Conflict of Interest

The authors declare no conflict of interest.

Data Availability Statement

The data that support the findings of this study are available from the corresponding author upon reasonable request.

Keywords

hydrogen bonding, near ambient pressure XPS, nitrogen doping, spectromicroscopy, surface chemistry

Received: April 17, 2024
Revised: May 21, 2024
Published online: June 10, 2024

[1] J. Zhao, G. Gorbatovski, O. Oll, E. Anderson, E. Lust, *Electrochim. Acta.* **2022**, *415*, 140263.
[2] O. Björneholm, M. H. Hansen, A. Hodgson, L.-M. Liu, D. T. Limmer, A. Michaelides, P. Pedevilla, J. Rossmeisl, H. Shen, G. Tocci, E. Tyrode, M.-M. Walz, J. Werner, H. Bluhm, *Chem. Rev.* **2016**, *116*, 7698.
[3] Q. Qin, M. Oschatz, *ChemElectroChem.* **2020**, *7*, 878.
[4] F. Béguin, V. Presser, A. Balducci, E. Frackowiak, *Adv. Mater.* **2014**, *26*, 2219.
[5] T. Wang, Y. Zhang, B. Huang, B. Cai, R. R. Rao, L. Giordano, S.-G. Sun, Y. Shao-Horn, *Nat. Catal.* **2021**, *4*, 753.
[6] R. Zhang, P. E. Pearce, Y. Duan, N. Dubouis, T. Marchandier, A. Grimaud, *Chem. Mater.* **2019**, *31*, 8248.
[7] F. G. Alabarse, B. Baptiste, M. Jiménez-Ruiz, B. Coasne, J. Haines, J.-B. Brubach, P. Roy, H. E. Fischer, S. Klotz, L. E. Bove, *J. Phys. Chem. C.* **2021**, *125*, 14378.
[8] H. Tian, J. Liang, J. Liu, *Adv. Mater.* **2019**, *31*, 1903886.
[9] Y. Li, J. Kim, J. Wang, N.-L. Liu, Y. Bando, A. A. Alshehri, Y. Yamauchi, C.-H. Hou, K. C.-W. Wu, *Nanoscale.* **2018**, *10*, 14852.
[10] W. Ju, A. Bagger, G.-P. Hao, A. S. Varela, I. Sinev, V. Bon, B. Roldan Cuenya, S. Kaskel, J. Rossmeisl, P. Strasser, *Nat. Commun.* **2017**, *8*, 944.
[11] G. P. Hao, G. Mondin, Z. Zheng, T. Biemelt, S. Klosz, R. Schubel, A. Eychmüller, S. Kaskel, *Angew. Chem., Int. Ed.* **2015**, *54*, 1941.
[12] H. Shao, Y.-C. Wu, Z. Lin, P.-L. Taberna, P. Simon, *Chem. Soc. Rev.* **2020**, *49*, 3005.
[13] C. Neto, H. T. T. Pham, R. Omnée, A. Canizarès, A. Slodczyk, M. Deschamps, E. Raymundo-Piñero, *ACS Appl. Mater. Interfaces.* **2022**, *14*, 44405.
[14] M. Perovic, Q. Qin, M. Oschatz, M. Perovic, Q. Qin, M. Oschatz, *Adv. Funct. Mater.* **2020**, *30*, 1908371.
[15] I. K. Ilic, M. Oschatz, I. K. Ilic, M. Oschatz, *Small.* **2021**, *17*, 2007508.
[16] L. Borchardt, Q. L. Zhu, M. E. Casco, R. Berger, X. Zhuang, S. Kaskel, X. Feng, Q. Xu, *Mater. Today.* **2017**, *20*, 592.
[17] R. Walczak, B. Kurpil, A. Savateev, T. Heil, J. Schmidt, Q. Qin, M. Antonietti, M. Oschatz, *Angew. Chem., Int. Ed.* **2018**, *57*, 10765.
[18] J. Mahmood, E. K. Lee, M. Jung, D. Shin, I. Y. Jeon, S. M. Jung, H. J. Choi, J. M. Seo, S. Y. Bae, S. D. Sohn, N. Park, J. H. Oh, H. J. Shin, J. B. Baek, *Nat. Commun.* **2015**, *6*, 6486.
[19] Z. Tian, N. López-Salas, C. Liu, T. Liu, M. Antonietti, *Adv. Sci.* **2020**, *7*, 2001767.
[20] W. Zhang, S. Zhan, Q. Qin, T. Heil, X. Liu, J. Hwang, T. H. Ferber, J. P. Hofmann, M. Oschatz, *Small.* **2022**, *18*, 2204116.
[21] R. Walczak, A. Savateev, J. Heske, N. V. Tarakina, S. Sahoo, J. D. Epping, T. D. Kühne, B. Kurpil, M. Antonietti, M. Oschatz, *Sustainable Energy Fuels.* **2019**, *3*, 2819.
[22] S. Du, D. Leistenschneider, J. Xiao, J. Dellith, E. Troschke, M. Oschatz, *ChemistryOpen.* **2022**, *11*, e202200193.
[23] J. Heske, R. Walczak, J. D. Epping, S. Youk, S. K. Sahoo, M. Antonietti, T. D. Kühne, M. Oschatz, *J. Mater. Chem. A.* **2021**, *9*, 22563.
[24] D. Lyu, K. Märker, Y. Zhou, E. W. Zhao, A. B. Gunnarsdóttir, S. P. Niblett, A. C. Forse, C. P. Grey, *J. Am. Chem. Soc.* **2024**, *146*, 9897.
[25] S. Burikov, T. Dolenko, S. Patsaeva, Y. Starokurov, V. Yuzhakov, *Mol. Phys.* **2010**, *108*, 2427.
[26] T. Petit, M. Lounasvuori, A. Chemin, P. Bärmann, *ACS Phys. Chem. Au.* **2023**, *3*, 263.
[27] M. Lounasvuori, T. Zhang, Y. Gogotsi, T. Petit, *J. Phys. Chem. C.* **2024**, *128*, 2803.
[28] D. Kim, E. Kim, S. Park, S. Kim, B. K. Min, H. J. Yoon, K. Kwak, M. Cho, *Chem.* **2021**, *7*, 1602.
[29] Y. Wang, T. Seki, X. Yu, C. C. Yu, K. Y. Chiang, K. F. Domke, J. Hunger, Y. Chen, Y. Nagata, M. Bonn, *Nature.* **2023**, *615*, E1.
[30] A. Montenegro, C. Dutta, M. Mammetkuliev, H. Shi, B. Hou, D. Bhattacharyya, B. Zhao, S. B. Cronin, A. V. Benderskii, *Nature.* **2021**, *594*, 62.
[31] P. Knittel, F. Buchner, E. Hadzifejzovic, C. Giese, P. Quellmalz, R. Seidel, T. Petit, B. Iliev, T. J. S. Schubert, C. E. Nebel, J. S. Foord, *ChemCatChem.* **2020**, *12*, 5548.
[32] J. Wu, Z. Liu, X. Lin, E. Jiang, S. Zhang, P. Huo, Y. Yan, P. Zhou, Y. Yan, *Nat. Commun.* **2022**, *13*, 6999.
[33] J. Ren, D. S. Achilleos, R. Golnak, H. Yuzawa, J. Xiao, M. Nagasaka, E. Reisner, T. Petit, *J. Phys. Chem. Lett.* **2019**, *10*, 3843.
[34] T. Petit, H. Yuzawa, M. Nagasaka, R. Yamanoi, E. Osawa, N. Kosugi, E. F. Aziz, *J. Phys. Chem. Lett.* **2015**, *6*, 2909.
[35] A. P. Hitchcock, M. Tronc, A. Modelli, *J. Phys. Chem.* **1989**, *93*, 3068.
[36] H. Zhang, X. Li, D. Zhang, L. Zhang, M. Kapilashrami, T. Sun, P.-A. Glans, J. Zhu, J. Zhong, Z. Hu, J. Guo, X. Sun, *Carbon.* **2016**, *103*, 480.
[37] J. Ren, L. Lin, K. Lieutenant, C. Schulz, D. Wong, T. Gimm, A. Bande, X. Wang, T. Petit, *Small Methods.* **2021**, *5*, 2000707.
[38] H. Yabuta, M. Uesugi, H. Naraoka, M. Ito, A. L. D. Kilcoyne, S. A. Sandford, F. Kitajima, H. Mita, Y. Takano, T. Yada, Y. Karouji, Y. Ishibashi, T. Okada, M. Abe, *Earth, Planets Space.* **2014**, *66*, 156.
[39] H. Yuzawa, M. Nagasaka, N. Kosugi, *J. Phys. Chem. C.* **2015**, *119*, 7738.
[40] B. Wu, H. Meng, D. M. Morales, F. Zeng, J. Zhu, B. Wang, M. Risch, Z. J. Xu, T. Petit, *Adv. Funct. Mater.* **2022**, *32*, 2204137.
[41] R. J. J. Jansen, H. V. Bekkum, *Carbon.* **1995**, *33*, 1021.
[42] J.-D. Förster, C. Gurk, M. Lamneck, H. Tong, F. Ditas, S. S. Steimer, P. A. Alpert, M. Ammann, J. Raabe, M. Weigand, B. Watts, U. Pöschl, M. O. Andreae, C. Pöhlker, *Atmosph. Measur. Techn.* **2020**, *13*, 3717.
[43] F. Frati, M. O. J. Y. Hunault, F. M. F. de Groot, *Chem. Rev.* **2020**, *120*, 4056.
[44] A. Nilsson, D. Nordlund, I. Waluyo, N. Huang, H. Ogasawara, S. Kaya, U. Bergmann, L.-Å. Näslund, H. Öström, P. Wernet, K. J. Andersson, T. Schiros, L. G. M. Pettersson, *J. Electron Spectrosc. Relat. Phenom.* **2010**, *177*, 99.
[45] P. Wernet, D. Nordlund, U. Bergmann, M. Cavalleri, M. Odelius, H. Ogasawara, L. Å. Näslund, T. K. Hirsch, L. Ojamäe, P. Glatzel, L. G. M. Pettersson, A. Nilsson, *Science.* **2004**, *304*, 995.
[46] D. Nordlund, H. Ogasawara, K. J. Andersson, M. Tatarkhanov, M. Salmerón, L. G. M. Pettersson, A. Nilsson, *Phys. Rev. B.* **2009**, *80*, 233404.
[47] M. Ekimova, C. Kleine, J. Ludwig, M. Ochmann, T. E. G. Agrenius, E. Kozari, D. Pines, E. Pines, N. Huse, P. Wernet, M. Odelius, E. T. J. Nibbering, *Angew. Chem., Int. Ed.* **2022**, *61*, e202211066.
[48] M. Nagasaka, H. Yuzawa, T. Horigome, N. Kosugi, *J. Electron Spectrosc. Relat. Phenom.* **2018**, *224*, 93.
[49] R. Cota, A. Tiwari, B. Ensing, H. J. Bakker, S. Woutersen, *Phys. Chem. Chem. Phys.* **2020**, *22*, 19940.
[50] A. Kuffel, J. Zielkiewicz, *J. Chem. Phys.* **2010**, *133*, 035102.
[51] Y. Qiu, L. Lupi, V. Molinero, *J. Phys. Chem. B.* **2018**, *122*, 3626.
[52] R. Follath, J. S. Schmidt, M. Weigand, K. Fauth, *AIP Conf. Proc.* **2010**, *1234*, 323.
[53] M. Lerotic, R. Mak, S. Wirick, F. Meirer, C. Jacobsen, *J. Synchrotron Radiat.* **2014**, *21*, 1206.
[54] C. Schulz, K. Lieutenant, J. Xiao, T. Hofmann, D. Wong, K. Habicht, *J. Synchrotron Radiat.* **2020**, *27*, 238.
[55] R. Signorell, *Phys. Rev. Lett.* **2020**, *124*, 205501.